Journal of Manufacturing Processes 73 (2022) 555–562

Contents lists available at ScienceDirect

Journal of Manufacturing Processes

journal homepage: www.elsevier.com/locate/manpro

Sensitivity of additively manufactured AA7075 to variation in feedstock composition and print parameters

Kasra Momeni

Department of Mechanical Engineering, University of Alabama, Tuscaloosa, AL 35487, United States

ARTICLE INFO

Keywords:
Additive manufacturing
Finite element analysis
CALPHAD
AA7075 alloy

ABSTRACT

We developed a combined finite element and CALPHAD based model of the Laser Powder Bed Fusion (LPBF) process for AA7075 alloy that considers the effect of feedstock composition and print parameters. A single-pass of a laser on a layer of AA7075 alloy powder has been considered. Sensitivity of temperature evolution and melt pool geometry to variation in the stoichiometry of the feedstock powder and laser source characteristics have been studied. Our results indicate that deviation (up to 10%) of the feedstock composition from the AA7075 raises the maximum temperature and increases melt pool size. Excess Cu content shows the largest melt pool width and depth among all the cases. The peak temperature is higher than the standard feedstock composition in all cases, except when the Cu concentration is reduced. Increasing the scan power also results in a higher peak temperature and a larger melt pool size. Furthermore, the temperature's rise time increases by lowering the scan speed.

1. Introduction

Additive manufacturing (AM) has been widely implemented to produce parts for applications in aerospace, automotive, rapid prototyping, and various manufacturing industries. The ability to construct parts layer by layer from a computer-aided drawing enables the economical manufacturing of complex parts and allows greater design flexibility [1–4]. In particular, additive manufacturing techniques allow control over material microstructure and composition variation as the parts are manufactured. Thus, adding a new dimension to the design space, i.e., manufacturing parts with tailored functionalities and properties [5–7]. Laser powder bed fusion (LPBF) is an additive manufacturing technology commonly used for producing functional metal components [8,9]. The process utilizes a laser heat source to melt the metal powder layers at specified locations, thus building the component layer by layer. Despite the unprecedented degrees of freedom and manufacturing flexibility of the LPBF method, this process is limited to printing only a few alloys. This limitation is due to unsuitable microstructures, such as columnar grains and cracks, during rapid melting and solidification [8–10]. On the other hand, aluminum alloys' additive manufacturing is crucial in the aerospace and automotive industries due to their high-performance mechanical properties and processability [2,9,11–13]. Much effort has been dedicated to finding alloys with suitable properties and optimizing AM process parameters. The exhaustive trial and error experimentations are prohibited due to significant time and costs. Analytical and computational models provide an alternative approach for designing and optimizing process parameters and alloy compositions [1,14–20,42–47].

Here, we developed a heat transfer-based model of the LPBF for AA7075 that consists of two parts: (i) calculating material properties for various alloy compositions using available material databases, such as Thermo-Calc [17,21,22], and (ii) thermophysical modeling of the LPBF process. We obtained material properties such as temperature-dependent density, heat capacity, and solidus/liquidus temperature from CALPHAD based simulations and corresponding thermodynamic and mobility databases [16,17,21–27]. However, thermal conductivity data could not be obtained from the aforementioned tools and collected from the literature [15,21]. Capitalizing on previous efforts [14,15,17,18,22,28–33], we developed a finite element (FE) analysis-based model to calculate the temperature evolution and melt pool geometry [14,15,17,18,22,28–33]. The laser's heat flux is modeled using a gaussian surface, which shines in the normal direction to the substrate [17,22,31]. Appropriate boundary conditions are assumed for the thermal model to resemble actual experimental conditions (see Section 2.1) [15,17].

Table 1 shows the reference composition of AA7075 alloy for which material properties such as density, specific heat capacity, and liquidus/solidus temperature were calculated using Thermocalc and

E-mail address: kmomeni@ua.edu.

https://doi.org/10.1016/j.jmapro.2021.11.026
Received 28 June 2021; Received in revised form 7 November 2021; Accepted 13 November 2021
Available online 23 November 2021
1526-6125/

corresponding Aluminum TCAL6 thermodynamic and MOBAL5 mobility databases. Some material properties such as thermal conductivity, power bed absorption coefficient, and emissivity were acquired from the literature [15]. We further analyzed the effect of variation in the feedstock composition by changing the mass fraction of the three solutes with the most prominent content, i.e., Zn, Mg, and Cu.

We performed thermal analysis using COMSOL Multiphysics software [35] and material property data obtained from CALPHAD based simulations and literature. We established separate property data sets for the substrate and powder layer using appropriate conversion techniques (see Section 2.3) [15,17,22]. We determined the temperature evolution and melt pool geometry for default process parameters of 200 W laser power and 2000 mms^{-1} laser scan speed. We further investigated process parameters' effect on the temperature profile and melt pool size of powder bed by varying laser power from 100 W to 300 W and laser scan speed from 1500 mms^{-1} to 2500 mms^{-1}. In order to analyze the accuracy of the model, we simulated AA6061 alloy and compared the results with experimental values listed in Ref. [1]. We also conducted a sensitivity analysis to determine the effect of control parameters, i.e., laser power and spot size, on the peak temperature of the powder bed. The thermal model developed here can be further enhanced with flow physics to account for the solidified powder layer's shape distortion.

2. Model development

We developed a nonlinear, transient heat transfer model coupled with phase transformation to calculate the temperature profile and melt pool geometry along the laser path, which we numerically solve using the FE technique. The model geometry consists of a 6 mm(length) × 1.4 mm (width) × 0.6 mm (thickness) solid substrate with a powder layer of 37 μm on the top surface. The FE model considered a single-pass laser scan parallel to the geometry's length and located at an offset of 50 μm from the top powder layer's center. Fig. 1 shows the geometry and mesh distribution of the model.

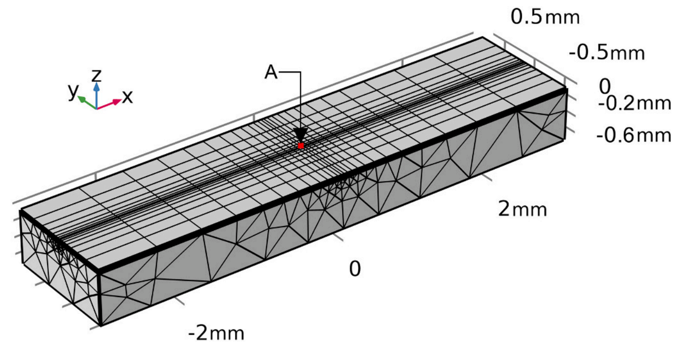

Fig. 1. Geometry and mesh distribution of the FE model. A finer mesh is implemented along the laser's path, while a coarser mesh is adopted for the rest of the geometry. Double geometric progression mesh refinement was used to create a denser mesh near the powder layer's center, where the temperature evolution will be calculated as the laser passes. The red dot represents point **A** (0, 50 μm, 0), where a probe has been placed to record the temperature evolution during the process. (For interpretation of the references to colour in this figure legend, the reader is referred to the web version of this article.)

2.1. Heat transfer model

Fourier's heat conduction law with an energy balance equation was used to model the heat transfer for the LPBF process [15,22,36], i.e.,

$$\frac{\partial(\rho c_p T)}{\partial t} = \nabla \bullet (\kappa \nabla \mathrm{T}) + \mathrm{Q} \tag{1}$$

Here, T is the time-dependent temperature field. The terms ρ, κ,and c_p are density, thermal conductivity, and specific heat capacity, respectively, which are assumed to be only a function of temperature T (see Fig. S.1 in supplementary materials). An initial uniform temperature of 353 K has been assumed throughout the entire geometry.

The boundary condition for the top layer surface consists of three main components, i.e., (i) the laser input heat that is represented by q_s, (ii) conduction, and (iii) radiation heat transfer,

$$(-\kappa \nabla T) \bullet \hat{\mathrm{n}} = \mathrm{q_s} + \mathrm{h}(\mathrm{T} - \mathrm{T_e}) + \varepsilon \sigma (\mathrm{T}^4 - \mathrm{T_e^4}) \tag{2}$$

Here, $\hat{n}$ indicates the surface normal, h is the convective heat transfer coefficient, ε and σ are the emissivity and Boltzmann constants, respectively, and T_e=293.15 K is the ambient temperature. Temperature-dependent emissivity data for powder and bulk state material was acquired from literature (see Fig. S.1 in supplementary materials) [15]. The value of h was assumed to be 0.05 W/m^2·K. We assumed adiabatic boundary conditions for all other boundaries other than the top surface.

2.2. Laser model

The laser and the top surface interaction is modeled as a moving heat source using a Gaussian surface expression [17,22]. The heat flux, q_s, associated with the laser heat source is

$$q_s = \frac{2AP}{\pi r_b^2} exp\left(\frac{-2r^2}{r_b^2}\right) \tag{3}$$

The laser power P varied from 100 W to 300 W, and absorption coefficient A was taken as 0.34 [37]. r_b represents the laser beam radius, which is set to 50 μm. The radial distance to the beam centerline, $\boldsymbol{r}$, is measured in μm, which can be calculated using the x-position and y-position of the beam's center coordinates at any given time, t, as $\boldsymbol{r} = \sqrt{(x - x_0)^2 + (y - y_0)^2}$. Here x_0 and y_0 are coordinates of the laser beam's center. The initial position of the laser is at (−1,0.05,0) [mm], it moves at a speed of 2000 mms^{-1} to its' final position at (1,0.05,0) [mm] [15].

2.3. Material properties

We calculated the temperature-dependent density and specific heat capacity of the AA7075 using Scheil's rapid solidification model [17,38]. We further used the Thermo-Calc software to calculate the liquidus temperature, $T_l = 1007.01$ K, and solidus temperature, $T_s = 777.67$ K, of the alloy AA7075 [38]. The powder's density and thermal conductivity are different from the corresponding bulk values [1,15,19,22]. A packing ratio φ=0.7 is introduced to relate the powder state density to bulk state density, ρ_{solid} [15]. The temperature-dependent density of the material is modeled as,

$$\rho(T) = \begin{cases} \varphi \bullet \rho_{solid}(T), T < T_l; before\ first\ melt \\ \rho_{solid}(T), T \geq T_l; first\ melt \\ \rho_{solid}(T), after\ first\ melt \end{cases} \tag{4}$$

Table 1
Composition of AA7075 Alloy [34].

Elements	Al	Zn	Mg	Cu	Fe	Si	Mn	Cr	Ti
Composition (Mass Percent)	88.0	6.1	2.6	1.6	0.55	0.4	0.3	0.28	0.2

The temperature-dependent thermal conductivity, $k(T)$, is given as [11,34].

$$\kappa(T) = \begin{cases} \kappa_{powder}(T), T < T_l; before\ first\ melt \\ \kappa_{solid}(T), T \geq T_l; first\ melt \\ \kappa_{solid}(T), after\ first\ melt \end{cases} \quad (5)$$

Switching from 'powder' to 'bulk' material property is performed using the irreversible transformation module in COMSOL. Once the liquidus temperature is reached for the first time in any mesh element, the material property switches irreversibly from powder to bulk property data set with a transformation time of 1 ps.

Mass percentages of the three major solute constituents, Zn, Mg, and Cu, were varied within a ± 10% range from the typical AA7075 alloy composition, Table 2, to understand the role of feedstock composition. We calculated the solidus/liquidus temperatures, density, and heat capacity of these alloys using Thermo-Calc [39]. It was observed that deviation from feedstock composition had the opposite effect on density and heat capacity for each case, i.e., for each case, if the density increased (decreased), then the heat capacity would be lowered (raised). The aforementioned material property values for the listed cases *A-F* are given in supplementary materials.

We assumed the alloy's thermal conductivity and absorption coefficient remain unchanged despite the change in solute compositions due to the unavailability of appropriate data. All the remaining constants and coefficients used for the simulation were kept the same. Separate simulations were run for each case to determine the effect of these composition variations on the temperature profile in the powder layer.

3. Numerical model

A transient heat transfer model was developed with numeric tools and computational technics. The CALPHAD based simulations were performed using Thermo-Calc software's Scheil calculator and property model calculator and corresponding TCAL6 thermodynamic and MOBAL5 mobility databases [39]. We defined the alloy compositions were in the system definer and used the coupled Scheil calculator and property model calculator to determine the density, heat capacity, and solidus/liquids temperature.

The FE analysis was performed using the heat transfer study of COMSOL Multiphysics, where we used the phase transforming material model to capture the powder to bulk melt transformation [35]. We used mesh elements of variable sizes to improve computational efficiency. For the powder layer, quadratic mesh elements were used. Here, the mesh elements along the laser path have a dense mesh, while a coarser mesh has been adopted for the rest of the geometry. The top powder layer was divided into 25, 15, and 5 quadratic elements along its length, width, and height, respectively, with a symmetric distribution of geometric sequence having 0.05, 0.08, and 0.5 element ratios to get a denser mesh along the laser path. A coarser tetrahedral mesh setting was implemented for the substrate layer with a 1.14 mm maximum and 0.24 mm minimum element size.

A time step of 1 ms was selected for the time-dependent study, which utilized a fully coupled PARDISO linear solver with a constant (Newton) nonlinear method. A damping factor of 0.9 was selected for the nonlinear method. Anderson acceleration scheme was also utilized with

Table 2
Variation of alloy composition for uncertainty analysis.

Case	Elements	Al	Zn	Mg	Cu	Unchanged
Feedstock	AA7075	88.00	6.10	2.60	1.60	1.70
A	Excess Zn	87.39	6.71	2.60	1.60	1.70
B	Reduced Zn	88.61	5.49	2.60	1.60	1.70
C	Excess Mg	87.74	6.10	2.86	1.60	1.70
D	Reduced Mg	88.26	6.10	2.34	1.60	1.70
E	Excess Cu	87.84	6.10	2.60	1.76	1.70
F	Reduced Cu	88.16	6.10	2.60	1.44	1.70

a dimension of iteration space of 5 and a mixing factor of 0.9. We used the quadratic Lagrange shape function. We ran separate simulations with denser mesh settings and compared the results to investigate mesh dependence. The analysis showed no significant evidence of mesh dependence for both feedstock AA7075 and varied composition cases.

3.1. Sensitivity analysis

We calculated the sensitivity of the peak temperature of the powder bed concerning control parameters laser power and spot size using a separate stationary solver. The temperature *T(t)* at any point in the domain is related to the input laser heat flux q_s through Eq. (1) and Eq. (3). On the other hand, the heat flux q_s is directly a function of laser power P and laser spot size r_b. That indicates,

$$T(t) = f(q_s) = f(P, r_b) \quad (6)$$

$$\frac{\partial T}{\partial P} = \frac{\partial T}{\partial q_s} \times \frac{\partial q_s}{\partial P} \quad (7)$$

$$\frac{\partial T}{\partial r_b} = \frac{\partial T}{\partial q_s} \times \frac{\partial q_s}{\partial r_b} \quad (8)$$

The sensitivity of peak temperature to laser power ($\partial T/\partial P$) and laser spot size ($\partial T/\partial r_b$) was calculated at point ***A*** (0, 50 μm, 0) where the probe is placed. We set up the sensitivity module configuration using an adjoint gradient method with a stationary study step. We collected boundary temperature and powder melt history data from the time-dependent study at steady-state conditions and used them as initial and boundary conditions to set up the stationary solver. We kept the top powder layer's heat flux and boundary conditions the same as the time-dependent study. The rest of the boundaries had temperatures from the time-dependent solution set as boundary conditions.

4. Experimental validation

The most comprehensive study related to the proposed model for an alloy with a composition closest to AA7075 is presented in Ref. [1], which focuses on AA6061. We validated our proposed model by adjusting it to AA6061, where our model showed a close correlation with reported experimental measurements for the AA6061. Subsequently, we used the validated model to study AA7075 and its sensitivity to print parameters. Ref. [1] reported melt pool width and depth for a single track laser scan on a 50 μm (thickness) AA6061 alloy powder bed. The laser spot size was 80 μm (diameter), and the laser power and scan speed were 150 W and 1140 mm/s, respectively. The aforementioned configurations determined melt pool width between 61.62–106.24 μm and melt pool depth between 14.69–26.23 μm (Fig. 2).

We replicated similar conditions using our model by calculating and gathering AA6061 material properties from CALPHAD simulations and corresponding literature [40,41]. The print parameters (layer thickness, laser spot size, power, and scan speed) were replicated using reported values in Ref. [1]. Our simulations calculated melt pool width and depth of ~121.458 μm and ~47.73 μm, respectively (see Fig. S.4 in supplementary materials). Although the simulation results closely correspond with the experimental values of Ref. [1], our numerical model overestimates the melt pool width/depth. The computational model does not account for evaporation of the materials as peak temperature exceeds the boiling temperature of the alloy constituents, which explains this discrepancy.

5. Results and discussion

We took the data from a probe placed at ***A*** (0, 50 μm, 0) on the laser path to plot the powder layer's temperature profile during the LPBF process. Fig. 3 shows the temperature profile at point ***A*** over the total simulation period. The maximum temperature reached 2819.20 K at $t =$

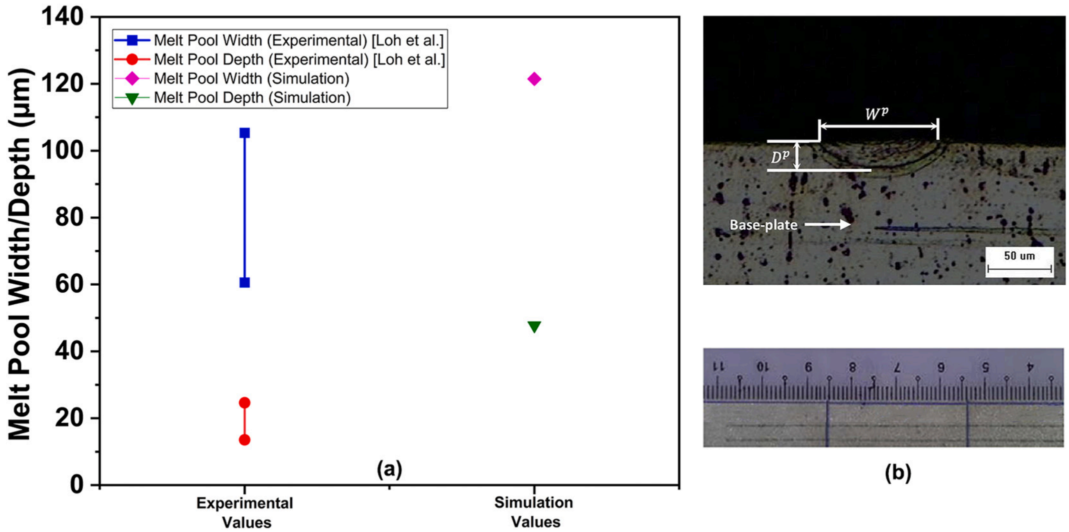

Fig. 2. Simulation vs. experimental results for AA6061 alloy. The simulation was performed at $P = 150$ W, and V = 1140 mms^{-1} for a 50 µm AA6061 powder bed, and the melt pool width and depth were ~ 121.458 µm and ~ 47.73 µm, respectively. (a) shows the experimental values acquired from Ref. [1], which reported melt pool width in the range of 61.62–106.24 µm and depth in the range of 14.69–26.23 µm for the similar printing conditions. (b) shows the measurement of melt pool dimension (adapted from Ref. [1] with permission from Elsevier).

0.503 ms, and the rise time was ~0.075 ms. As the laser beam passed over point *A*, the temperature sharply drops. The sudden change in the rate of cooling as the temperature reaches $T_l = 1007.01$ K can be accounted for by the phase change from melt to solid of the material. Fig. 4 (a) shows the temperature gradient along the geometry's length, and Fig. 4 (b) shows the melt pool transverse to the laser path at $t = 0.51$ ms. We assumed that melt (solid) forms when the temperature exceeds (drops below) the liquidus (solidus) temperature. We calculated the melt pool width and depth for AA7075 to be ~0.128 mm and ~ 42 µm, respectively (see Fig. S.5 (c) in supplementary materials).

The sensitivity of peak temperature to laser power and spot size is shown in Fig. 5. Separate simulations were performed at 100 W ~ 300 W to calculate the sensitivity of the peak temperature to laser power and spot size. As power is increased from 100 W to 300 W, the sensitivity of the peak temperature remained primarily unchanged for control both parameters, except for the 150 W case, which had the highest sensitivity to laser power (8.7221 K/W) and spot size (−35.229 K/W). Sensitivity values for the rest of the cases are listed in Table S.2 in supplementary materials.

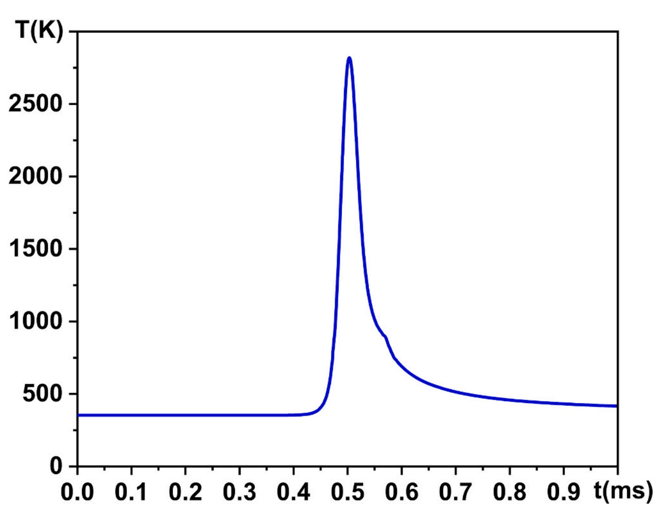

Fig. 3. Temperature profile at point A along the laser path. For $P = 200$ W and a laser scan speed of 2000 mms^{-1}. The peak temperature reaches 2819.20 K with a rise time of approximately 0.075 ms.

5.1. Effect of laser power

The change in laser power influences the temperature distribution and thus the melt pool dimensions, Fig. 6. The peak temperature increases from 1606.88 K to 4053.63 K as laser power increased from 100 W to 300 W. However, increasing laser power did not affect the rise time of peak temperature and duration of melt. Having a peak temperature higher than the boiling temperatures of the alloy constituents will cause the evaporation of material which may change alloy composition and degrade material characteristics. So, the peak temperature must not exceed the lowest boiling temperature among the alloy constituents excessively.

The melt pool's width and depth also increase by increasing the laser power, Fig. 7. The melt pool width doubles from 0.085 mm to 0.177 mm as power increases from 100 W to 300 W. Melt pool geometry for 150 W ~ 250 W settings follows similar width and depth trends (see Fig. S.5 supplementary materials). While having a larger melt pool width decreases print time, it often distorts the part geometry and pore spaces to form within the part. Therefore, laser power has to be calibrated precisely to achieve optimum melt pool geometry.

5.2. Effect of laser scan speed

The laser scan speed influences the peak temperature and rise/fall times in the temperature profile, Fig. 8. The peak temperature drops by ~249 K as the laser scan speed increased from 1500 mms^{-1} to 2500 mms^{-1}. However, the more significant effect of increasing scan speed is the decrease in the temperature profile's rise and fall time.

Laser scan speed also affects the geometry of the melt pool. With increased speed, the melt pool's depth and width decrease, Fig. 9. The melt pool width and depth reduce by ~0.018 mm and ~ 0.010 mm, respectively, as the laser speed varies from 1500 mm/s to 2500 mm/s. Thus, it is evident that laser scan speed has a more prominent effect on the melt pool's width than its depth. We performed additional simulations for 1750 mm/s to 2250 mm/s laser scan speeds, following similar depth reduction trends (see Fig. S.5 in supplementary materials).

5.3. Effect of feedstock composition

Except for *Case F,* the variation of the solute mass percent from the typical AA7075 alloy composition increased peak temperature. Fig. 10

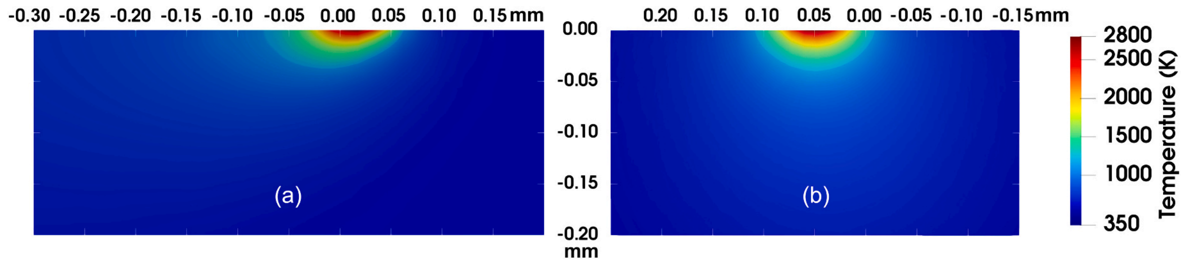

Fig. 4. Temperature distribution for P = 200 W and V = 2000 mms^{-1}. (a) Temperature profile along the laser path, and (b) transverse to laser path at point A at $t =$ 0.51 ms.

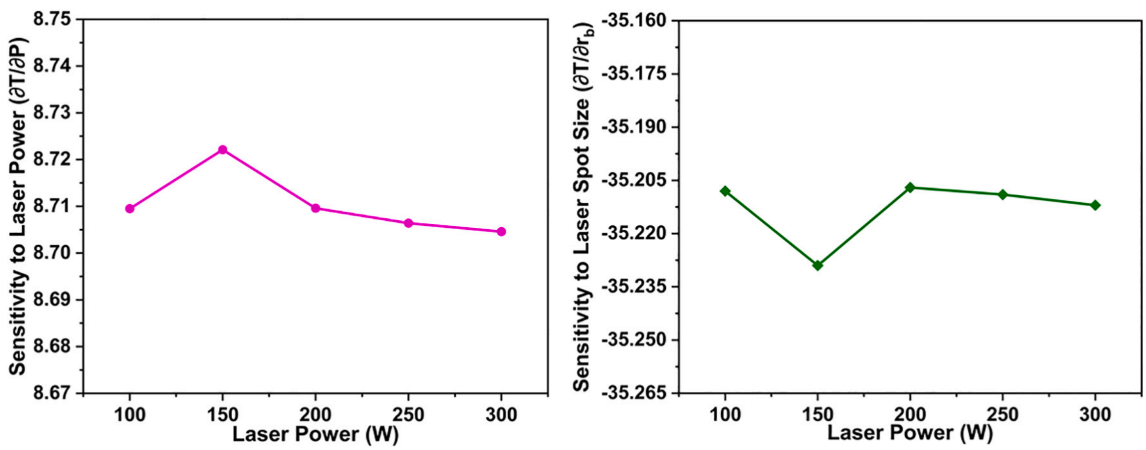

Fig. 5. Sensitivity of the peak temperature at point *A* with respect to laser power and spot size. Values are taken at different input powers. Both sensitivities remain primarily unchanged as laser power is varied from 100 W to 300 W except 150 W, which had the highest sensitivity to laser power and scan speed.

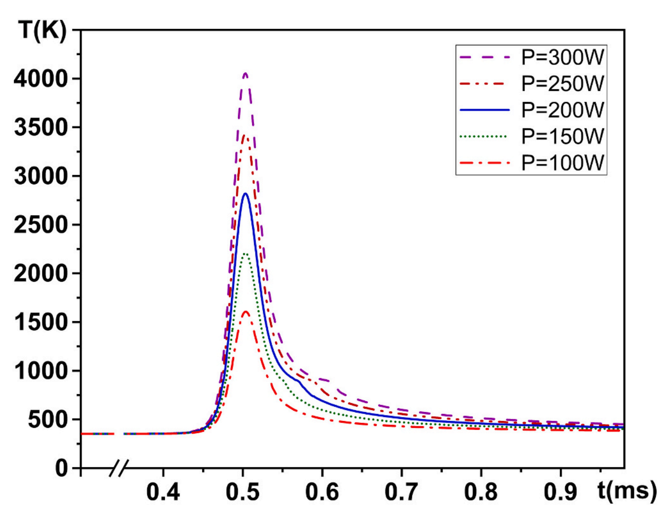

Fig. 6. Temperature profile at point "A" along the laser path for various powers. For a constant laser scan speed of 2000 mms^{-1}, the peak temperature rises from 1606.88 K to 4053.63 K as the power increases from 100 W to 300 W.

shows the effect of Zn mass percent variation (±10% mass fraction of the AA7075) on the powder layer's overall temperature evolution. The peak temperature for feedstock AA7075 was 2819.20 K. Both the increase and the decrease of Zn mass percent resulted in increased peak temperature. For *Case A* and *Case B,* representing a 10% increase and decrease of Zn concerning the AA7075 composition (Table 2), the recorded peak temperature was 2861.11 K and 2833.39 K, respectively. The melt pool width and depth increased for both excess and reduced Zn cases (see Fig. S.6 in supplementary materials), with *Case A* having a more prominent effect. The rise and fall time, however, remained unchanged for both cases.

Fig. 11 illustrates the effect of Mg variation on the temperature evolution in the powder layer. It indicates that reducing the Mg content results in a higher peak temperature. For both Case C and Case D, where the mass percent of Mg was increased and decreased by ±10%, respectively, the peak temperature increased to 2858.69 K and 2869.61 K from 2819.20 K for AA7075. Furthermore, the melt pool width and depth were higher for the reduced Mg composition (see Fig. S.6 in supplementary materials).

Similar to the cases above, the Cu content increase also resulted in a peak temperature rise. Fig. 12 shows the effect of Cu's mass percent variation on the temperature evolution in the powder layer. For *Case-E* representing a 10% increase in Cu composition, the peak temperature was 2895.60 K. However, in *Case-F,* with a 10% reduced Cu composition, the peak temperature was recorded at 2817.27 K, similar to the feedstock composition value of 2819.20 K. The excess Cu case also had the largest melt pool width ~0.133 mm and depth ~0.049 mm. In contrast, for the reduced Cu condition, the geometry was similar to the feedstock composition. Melt pool geometry for *case A-F* is listed in supplementary materials.

6. Conclusion

We developed a combined CALPHAD and FE model of a single-track LPBF process for AA7075 alloy, which is of interest due to its optimum mechanical properties and processability, specifically aerospace applications. The developed tool demonstrated excellent potential for predicting material properties and process parameter optimization in additive manufacturing processes. We have calculated temperature-dependent material properties, including density and heat capacity. In addition, the temperature profile along the laser path and the melt pool

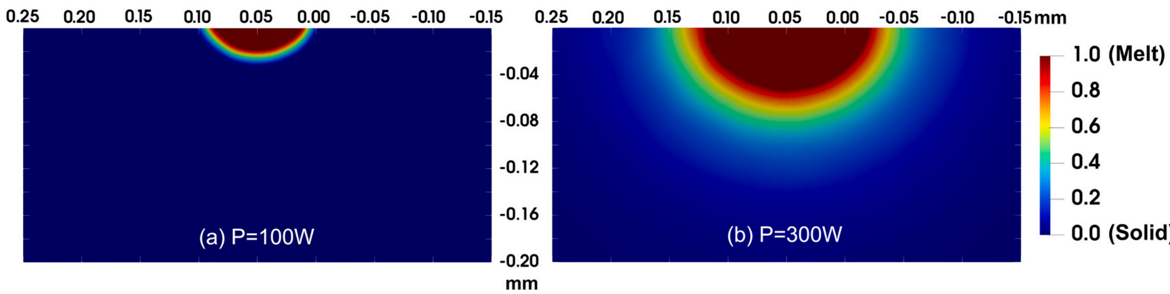

Fig. 7. Melt pool geometry as laser power is varied. Values are taken at point A along the laser path at $t = 0.51$ ms. The melt pool width and depth increase by ~0.092 mm and ~ 0.041 mm as power increases from (a) 100 W to (b) 300 W.

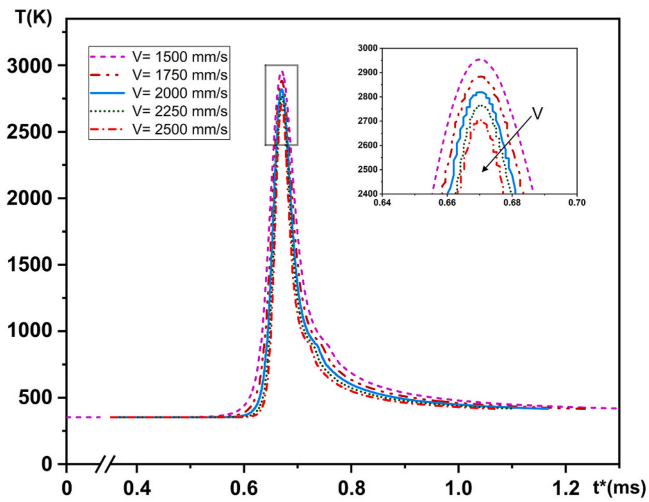

Fig. 8. Temperature vs. normalized time profile at point A situated along the laser path for various laser scan speeds. Profiles are normalized concerning the peak temperature reaching time ($t = 0.67$ ms) for V = 1500 mms^{-1} with a constant power of 200 W. As the laser scan speed increases from 1500 mms^{-1} to 2500 mms^{-1}, the profile's peak temperature decreases by ~249 K and reduces the rise/fall time.

transverse to the path were investigated for different process parameters.

A laser power of 200 W with a scan speed of 2000 mm/s has been reported as the suitable conditions for printing AA7075 alloy using the LBPF process [11]. We recorded a maximum temperature of 2819.20 K at point *A* using these values in our simulation. The melt pool width and depth were approximately 0.128 mm and 42 μm for this case.

Process parameters such as laser power and laser scan speed affect the temperature evolution of the powder bed. The temperature profile and melt pool geometry for laser power settings ranging from 100 W to 300 W and laser scan speed ranging from 1500 mm/s to 2500 mm/s were investigated. Varying laser power had a significant impact on maximum temperature evolution and melt pool size. The maximum temperature dropped to 1606.88 K from 4053.63 K as power was lowered from 300 W to 100 W. Melt pool width and depth were also reduced by the decrease in power setting. The peak temperature and melt pool depth decreased with the increase in laser scan speed. The peak temperature dropped by ~248.96 K as speed was increased from 1500 mm/s to 2500 mm/s.

Contrary to power variation, changing the speed influenced the rise and fall time of the temperature profile, where rise time was reduced at a higher speed setting. As for the melt pool geometry, speed seems to have a more prominent effect on melt pool width rather than depth. Furthermore, we performed a sensitivity analysis to understand the

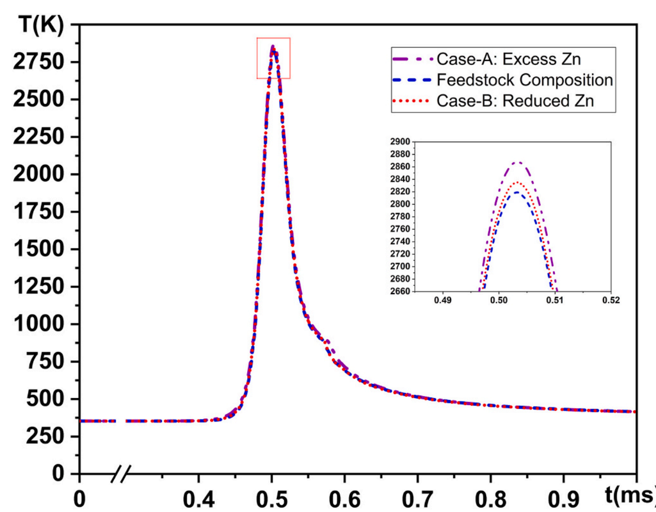

Fig. 10. Effect of Zn composition variation. The mass percentage of Zn was varied within the ±10% range. For both cases, the peak temperature increased compared to AA7075. The peak temperatures were 2861.11 K and 2833.39 K for Case A and Case B, respectively.

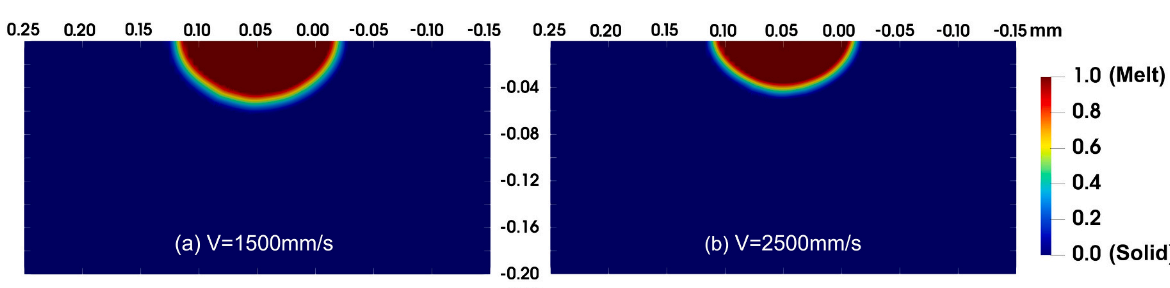

Fig. 9. Melt pool geometry for different laser scan speeds. Melt pool size along the laser path at peak temperature, indicating that the melt pool width decreases more significantly (~0.018 mm) than the depth (~0.010 mm) as speed is increased from (a) 1500 mm/s to (b) 2500 mm/s.

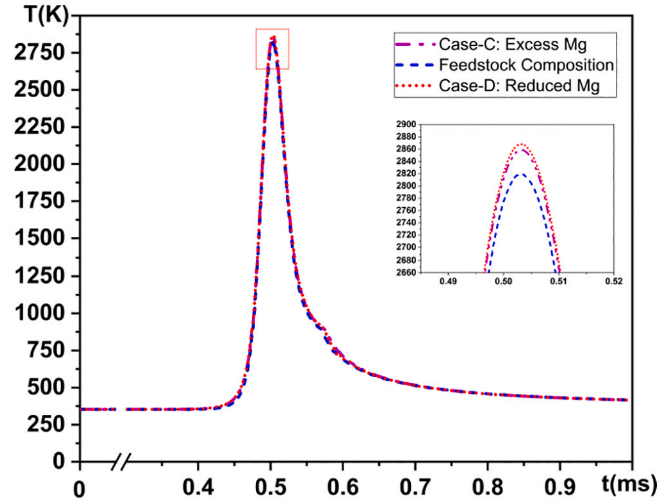

Fig. 11. Effect of Mg composition variation. The mass percentage of Mg was varied within the ±10% range. The peak temperatures were 2858.69 K and 2869.61 K for Case C and Case D, respectively. For both cases, the peak temperature was higher compared to AA7075.

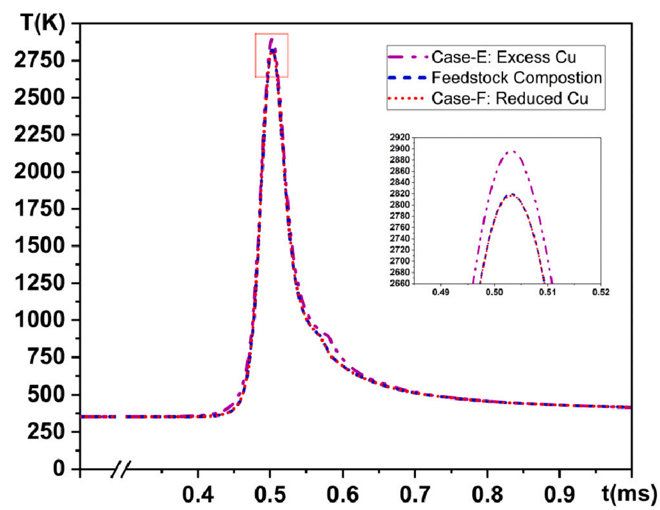

Fig. 12. Effect of Cu composition variation. The mass percentage of Cu was varied within the ±10% range. The peak temperature increased for the excess Cu composition only. The peak temperatures were 2895.60 K and 2817.27 K for Case E and Case F, respectively.

effect of change in the laser power and spot size on the maximum temperature. Our findings indicate that the sensitivity of the peak temperature to both laser power and spot size varies within a minimal range as we increase the laser power. The 150 W power setting had the highest sensitivity to laser power (8.7221 K/W) and spot size (−35.229 K/W) among the 100 W ~ 300 W range.

We determined the effect of variation in the concentration of three major solute elements Zn, Mg, and Cu. As the mass percent for each aforementioned element was varied within the ±10% range, for all cases except *Case F*, the peak temperature increased from the reference AA7075 composition value of 2819.20 K, and melt pool size increased. *Case F*, which represents 10% reduced Cu composition, had the lowest peak temperature of 2817.27 K with similar melt pool geometry. We can obtain more accurate results with appropriate thermal conductivity data for the variant compositions.

Declaration of competing interest

The authors declare that they have no known competing financial interests or personal relationships that could have appeared to influence the work reported in this paper.

Acknowledgment

This project is partly supported by DoE-ARPA-E OPEN (DE-AR0001066), NASA-EPSCoR, the University of Alabama, and the NSF-CAREER under the NSF cooperative agreement CBET-2042683. We also acknowledge the help of Dr. Shengmin Guo, Dr. Jonathan Raush, and S M Ashique Imran.

Appendix A. Supplementary data

Supplementary data to this article can be found online at https://doi.org/10.1016/j.jmapro.2021.11.026.

References

[1] Loh LE, Chua CK, Yeong WY, Song J, Mapar M, Sing SL, et al. Numerical investigation and an effective modelling on the selective laser melting (SLM) process with aluminium alloy 6061. Int J Heat Mass Transf 2015;80:288–300. https://doi.org/10.1016/j.ijheatmasstransfer.2014.09.014.

[2] Aboulkhair NT, Simonelli M, Parry L, Ashcroft I, Tuck C, Hague R. 3D printing of aluminium alloys: additive manufacturing of aluminium alloys using selective laser melting. Prog Mater Sci 2019;106:100578. https://doi.org/10.1016/j.pmatsci.2019.100578.

[3] Rowe RA, Tajyar A, Munther M, Johanns KE, Allison PG, Momeni K. Nanoscale serration characteristics of additively manufactured superalloys. J Alloys Compd 2021;854:156723. https://doi.org/10.1016/j.jallcom.2020.156723.

[4] Davami K, Mohsenizadeh M, Munther M, Palma T, Beheshti A, Momeni K. Dynamic energy absorption characteristics of additivelymanufactured shape-recovering lattice structures. Mater Res Express 2019;6. https://doi.org/10.1088/2053-1591/aaf78c.

[5] Maietta S, Gloria A, Improta G, Richetta M, De Santis R, Martorelli M. A further analysis on Ti6Al4V lattice structures manufactured by selective laser melting. J Healthc Eng 2019;2019.

[6] Momeni K, SMM Mofidian, Bardaweel H. Systematic design of high-strength multicomponent metamaterials. Mater Des 2019:183. https://doi.org/10.1016/j.matdes.2019.108124.

[7] Zhang C, Chen F, Huang Z, Jia M, Chen G, Ye Y. Additive manufacturing of functionally graded materials: A review. Mater Sci Eng A 2019;764:138209. https://doi.org/10.1016/j.msea.2019.138209.

[8] Roberts CE, Bourell D, Watt T, Cohen J. A novel processing approach for additive manufacturing of commercial aluminum alloys. Phys Procedia 2016;83:909–17. https://doi.org/10.1016/j.phpro.2016.08.095.

[9] Martin JH, Yahata BD, Hundley JM, Mayer JA, Schaedler TA, Pollock TM. 3D printing of high-strength aluminium alloys. Nature 2017;549:365–9. https://doi.org/10.1038/nature23894.

[10] Kumara C, Segerstark A, Hanning F, Dixit N, Joshi S, Moverare J, et al. Microstructure modelling of laser metal powder directed energy deposition of alloy 718. Addit Manuf 2019;25:357–64. https://doi.org/10.1016/j.addma.2018.11.024.

[11] Schmidtke K, Palm F, Hawkins A, Emmelmann C. Process and mechanical properties: applicability of a scandium modified Al-alloy for laser additive manufacturing. Phys Procedia 2011;12:369–74. https://doi.org/10.1016/j.phpro.2011.03.047.

[12] Bartkowiak K, Ullrich S, Frick T, Schmidt M. New developments of laser processing aluminium alloys via additive manufacturing technique. Phys Procedia 2011;12:393–401. https://doi.org/10.1016/j.phpro.2011.03.050.

[13] Montero Sistiaga ML, Mertens R, Vrancken B, Wang X, Van Hooreweder B, Kruth J-P, et al. Changing the alloy composition of Al7075 for better processability by selective laser melting. J Mater Process Technol 2016;238:437–45. https://doi.org/10.1016/j.jmatprotec.2016.08.003.

[14] Khairallah SA, Anderson AT, Rubenchik A, King WE. Laser powder-bed fusion additive manufacturing: Physics of complex melt flow and formation mechanisms of pores, spatter, and denudation zones. Acta Mater 2016;108:36–45. https://doi.org/10.1016/j.actamat.2016.02.014.

[15] Romano J, Ladani L, Sadowski M. Thermal modeling of laser based additive manufacturing processes within common materials. Procedia Manuf 2015;1:238–50. https://doi.org/10.1016/j.promfg.2015.09.012.

[16] Shi R, Luo AA. Applications of CALPHAD modeling and databases in advanced lightweight metallic materials. Calphad Comput Coupling Phase Diagrams Thermochem 2018;62:1–17. https://doi.org/10.1016/j.calphad.2018.04.009.

[17] Ghosh S, Ma L, Lane BM, Zhang F, et al. Application of finite element, phase-field, and CALPHAD-based methods to additive manufacturing of ni-based superalloys. Acta Mater 2017;139(15):244–53.

[18] Gusarov AV, Smurov I. Modeling the interaction of laser radiation with powder bed at selective laser melting. Phys Procedia 2010;5:381–94. https://doi.org/10.1016/j.phpro.2010.08.065.

[19] Zhang Z, Huang Y, Rani Kasinathan A, Imani Shahabad S, Ali U, Mahmoodkhani Y, et al. 3-Dimensional heat transfer modeling for laser powder-bed fusion additive manufacturing with volumetric heat sources based on varied thermal conductivity and absorptivity. Opt Laser Technol 2019;109:297–312. https://doi.org/10.1016/j.optlastec.2018.08.012.

[20] Hodge NE, Ferencz RM, Solberg JM. Implementation of a thermomechanical model for the simulation of selective laser melting. Comput Mech 2014;54:33–51. https://doi.org/10.1007/s00466-014-1024-2.

[21] Mason P, Hope A, Grundy AN. Applications of CALPHAD based tools to additive manufacturing. In: 2018 Stock User Gr Meet; 2018. p. 26.

[22] Ma L, Fong J, Lane B, Moylan S, JFI Solid. Using design of experiments in finite element modeling to identify critical variables for laser powder bed fusion. In: Res; 2015. n.d.

[23] Kattner UR. The calphad method and its role in material and process development. Technol Em Metal Mater e Min 2016;13:3–15. https://doi.org/10.4322/2176-1523.1059.

[24] Campbell CE, Kattner UR, Liu Z-K. The development of phase-based property data using the CALPHAD method and infrastructure needs. Integr Mater Manuf Innov 2014;3:158–80. https://doi.org/10.1186/2193-9772-3-12.

[25] Chen S-L, Cao W-S, Zhang F, Zhang C, Zhu J, Zhang J-Y. Development of a computational tool for materials design. Adv Manuf 2013;1:123–9. https://doi.org/10.1007/s40436-013-0021-6.

[26] Perrut M. Thermodynamic modeling by the CALPHAD method and its applications to innovative materials. AerospaceLab J 2015;9(1).

[27] Saunders N, Miodownik AP. CALPHAD (Calculation of Phase Diagrams) A Comprehensive Guide. 1st Edition1; 1998.

[28] Paul S, Motalab M, Zubaer MA, Hossain MZ. Strain rate and curing condition effects on the stress–strain behaviour of epoxy adhesive materials. J Adhes Sci Technol 2017:31. https://doi.org/10.1080/01694243.2017.1283109.

[29] Shiomi M, Yoshidome A, Abe F, Osakada K. Finite element analysis of melting and solidifying processes in laser rapid prototyping of metallic powders. Int J Mach Tool Manuf 1999;39:237–52.

[30] Kolossov S, Boillat E, Glardon R, Fischer P, Locher M. 3D FE simulation for temperature evolution in the selective laser sintering process. Int J Mach Tools Manuf 2004;44:117–23. https://doi.org/10.1016/j.ijmachtools.2003.10.019.

[31] Roberts IA, Wang CJ, Esterlein R, Stanford M, Mynors DJ. A three-dimensional finite element analysis of the temperature field during laser melting of metal powders in additive layer manufacturing. Int J Mach Tools Manuf 2009;49:916–23. https://doi.org/10.1016/j.ijmachtools.2009.07.004.

[32] Li C, Wang Y, Zhan H, Han T, Han B, Zhao W. Three-dimensional finite element analysis of temperatures and stresses in wide-band laser surface melting processing. Mater Des 2010;31:3366–73. https://doi.org/10.1016/j.matdes.2010.01.054.

[33] Li C, Gouge MF, Denlinger ER, Irwin JE, Michaleris P. Estimation of part-to-powder heat losses as surface convection in laser powder bed fusion. Addit Manuf 2019;26:258. https://doi.org/10.1016/j.addma.2019.02.006.

[34] MatWebTM . ASM Aerospace Specification Metals, Inc n.d. http://asm.matweb.com/search/SpecificMaterial.asp?bassnum=MA7075T6.

[35] COMSOL. Multiphysics Version 4.0 Released. Seal Technol2010; 2010. https://doi.org/10.1016/S1350-4789(10)70335-4.

[36] Carslaw HS, Jaeger JC. Conduction of Heat in Solids. Amen House, London E.C.4: Oxford University Press; 1946.

[37] Zaitsev AV, Ermolaev GV, Polyanskiy TA, Gurin AM. Numerical simulation of the shape of laser cut for fiber and CO2 lasers. AIP Conf Proc 2017;1893:30046. https://doi.org/10.1063/1.5007504.

[38] Helander T, Höglund L, Shi P, Sundman B. Thermo-Calc & DICTRA, computational tools for materials science. Calphad Comput Coupling Phase Diagrams Thermochem 2002;26:273–312. https://doi.org/10.1016/S0364-5916(02)00037-8.

[39] Andersson JO, Helander T, H Glund L, Shi P, Sundman B, Thermo-Calc DICTRA. In: Computational tools for materials science. 26; 2002. p. 273–312.

[40] Leitner M, Leitner T, Schmon A, Aziz K, Pottlacher G. Thermophysical properties of liquid aluminum. Metall Mater Trans A 2017;48:3036–45. https://doi.org/10.1007/s11661-017-4053-6.

[41] Wen C-D, Mudawar I. Experimental investigation of emissivity of aluminum alloys and temperature determination using multispectral radiation thermometry (MRT) algorithms. J Mater Eng Perform 2002;11:551–62. https://doi.org/10.1361/105994902770343818.

[42] Momeni K. Sensitivity of Laser Powder Bed Fusion Additive Manufactured HAYNES230 to Composition and Print Parameters. Journal of Materials Research and Technology 2021. In press.

[43] Momeni K, Levitas V. A phase-field approach to nonequilibrium phase transformations in elastic solids via an intermediate phase (melt) allowing for interface stresses. Physical Chemistry Chemical Physics 2016;18(17):12183–203.

[44] Momeni K, Levitas V. A phase-field approach to solid–solid phase transformations via intermediate interfacial phases under stress tensor. International Journal of Solids and Structures 2015;71:39–56.

[45] Momeni K, Levitas V, Warren J. The strong influence of internal stresses on the nucleation of a nanosized, deeply undercooled melt at a solid–solid phase interface. Nano letters 2015;15(4):2298–303.

[46] Momeni K, Levitas V. Propagating phase interface with intermediate interfacial phase: phase field approach. Physical Review B 2014;89(18):184102.

[47] Levitas V, Momeni K. Solid–solid transformations via nanoscale intermediate interfacial phase: Multiple structures, scale and mechanics effects. Acta materialia 2014;65:125–32.